Solar Phys (2016) 291:3269–3288
DOI 10.1007/s11207-016-1019-6

Transverse Oscillations in a Coronal Loop Triggered by a Jet

S. Sarkar[1] · V. Pant[2] · A.K. Srivastava[3] · D. Banerjee[2,4]

Received: 15 February 2016 / Accepted: 12 November 2016 / Published online: 21 November 2016

Abstract We detect and analyse transverse oscillations in a coronal loop, lying at the south–east limb of the Sun as seen from the *Atmospheric Imaging Assembly* (AIA) onboard the *Solar Dynamics Observatory* (SDO). The jet is believed to trigger transverse oscillations in the coronal loop. The jet originates from a region close to the coronal loop on 19 September 2014 at 02:01:35 UT. The length of the loop is estimated to be between 377 – 539 Mm. Only one complete oscillation is detected with an average period of about 32 ± 5 min. Using magnetohydrodynamic (MHD) seismologic inversion techniques, we estimate the magnetic field inside the coronal loop to be between 2.68 – 4.5 G. The velocity of the hot and cool components of the jet is estimated to be 168 km s^{-1} and 43 km s^{-1}, respectively. The energy density of the jet is found to be greater than the energy density of the oscillating coronal loop. We therefore conclude that the jet triggered transverse oscillations in the coronal loop. To our knowledge, this is the first coronal loop seismology study using the properties of a jet propagation to trigger oscillations.

Keywords Sun · Oscillations · Magnetic fields · Jets

Waves in the Solar Corona: From Microphysics to Macrophysics
Guest Editors: Valery M. Nakariakov, David J. Pascoe, and Robert A. Sych

Electronic supplementary material The online version of this article (doi:10.1007/s11207-016-1019-6) contains supplementary material, which is available to authorized users.

✉ D. Banerjee
dipu@iiap.res.in

S. Sarkar
shilpa@aries.res.in

V. Pant
vaibhav@iiap.res.in

1 Department of Physics, Presidency University, 86/1 College Street, Kolkata-73, India

2 Indian Institute of Astrophysics, Koramangala, Bangalore 560034, India

3 Indian Institute of Technology, Varanasi 221005, India

4 Center of Excellence in Space Sciences, IISER, Kolkata 741252, India

1. Introduction

Magnetohydrodynamic (MHD) waves are ubiquitous in the solar atmosphere. With the advent of high-resolution observations after the launch of the *Solar and Heliospheric Observatory* (SOHO), the *Transition Region and Coronal Explorer* (TRACE), *Hinode*, the *Solar Terrestrial Relations Observatory* (STEREO), and the *Solar Dynamics Observatory* (SDO), MHD waves have been well studied in recent years (Aschwanden *et al.*, 1999; Nakariakov *et al.*, 1999; Ofman and Wang, 2002; O'Shea *et al.*, 2007; Verwichte *et al.*, 2009; Srivastava and Dwivedi, 2010; Aschwanden and Schrijver, 2011; White and Verwichte, 2012; Mathioudakis, Jess, and Erdélyi, 2013).

The MHD waves and oscillations provide an important input in diagnosing the local plasma conditions using the principles of MHD seismology; as first suggested by Uchida (1970) using Moreton waves and Rosenberg (1970) using intensity fluctuations associated with type IV radio emission. Using the principles of MHD seismology, the magnetic field strength in the solar corona was estimated by Aschwanden *et al.* (1999, 2002), Nakariakov (2000), Nakariakov and Ofman (2001), Schrijver, Aschwanden, and Title (2002), Nakariakov and Verwichte (2005), Aschwanden (2006), Ruderman and Erdélyi (2009), and Aschwanden and Schrijver (2011).

Edwin and Roberts (1983) and Roberts, Edwin, and Benz (1984) interpreted transverse oscillations as a nearly incompressible fast kink mode in the MHD regime. The first observations of transverse oscillations in coronal loops were reported by Nakariakov *et al.* (1999), Aschwanden *et al.* (1999), and Schrijver *et al.* (1999). Transverse loop oscillations are often excited by nearby flares (Aschwanden *et al.*, 1999; Nakariakov *et al.*, 1999; Hori *et al.*, 2005; Verwichte, Foullon, and Van Doorsselaere, 2010; Wang *et al.*, 2012) and reconnection at the loop top (White and Verwichte, 2012). Other methods of measuring coronal magnetic field include gyro-resonance modelling of radio emission (Lee *et al.*, 1999), but this can only be applied to strong magnetic field regions like sunspots.

Transverse oscillations are often found to be damped most likely as a result of resonant absorption (Ruderman and Roberts, 2002; Goossens, Andries, and Aschwanden, 2002; Hollweg and Yang, 1988). Recently, there have been a few reports on decay-less oscillations in coronal loops (Nisticò, Nakariakov, and Verwichte, 2013; Anfinogentov, Nakariakov, and Nisticò, 2015). The driving mechanisms of such oscillations are not clearly understood. Recently, Zimovets and Nakariakov (2015) have provided a statistical investigation of coronal loop oscillations observed with SDO in association with blast waves that were due to a nearby flare, coronal mass ejections, type II radio bursts, etc. The authors found that kink oscillations ($\sim$95 % of them) were triggered by nearby low coronal eruptions (LCE) observed in the extreme ultraviolet band. Thus different types of transients can trigger oscillations in nearby magnetic structures, which provides additional data for coronal seismology. Here we explore whether transients such as jets, which carry much less energy than coronal mass ejections (CMEs) or blast waves, can trigger oscillations in nearby coronal loops.

In Section 2 we report the observations and the data analysis. In Section 3 we describe the observations from STEREO. In Section 4 we present a time–distance analysis to study the dynamics of the jet, which is followed by Section 5, where we carry out MHD seismology to estimate the magnetic field strength. In Section 6 we calculate the energy stored in jet and coronal loop oscillations. In Section 7 we report the coupling between oscillations in jets with coronal loop oscillations, which is followed by our conclusions.

2. Observations and Data Analysis

A jet was observed at the south–east limb of the Sun on 19 September 2014 at 02:01:35 UT. A narrow CME was detected at 04:37 UT with the *Large Angle Spectroscopic Coronagraph* (LASCO) onboard SOHO.[1] The CME may be the coronographic counterpart of the jet (Feng *et al.*, 2012; Paraschiv *et al.*, 2010; Nisticò *et al.*, 2009). The observation was made using the extreme ultraviolet (EUV) passbands of the *Atmospheric Imaging Assembly* (AIA) onboard SDO. The AIA instrument provides almost simultaneous full-disk images of the Sun at ten different wavelength bands, of which seven are in the EUV. AIA has a spatial resolution of 1.3″, a pixel size of 0.6″, and a cadence of 12 s (Lemen *et al.*, 2012). At 02:12:11 UT (∼ 12 min after the jet was started), transverse oscillations in a coronal loop were observed. The region where the jet and the coronal loop were observed is outlined with an orange box in Figure 1. The jet is marked with an arrow. A sequence of images was taken, encompassing 1.5 h, covering 1 min before and 1.48 h after the jet. Since the jet becomes fainter as it propagates outward, we made an unsharp mask movie to clearly show the propagation of the jet and its interaction with the coronal loop (see movie 1 online). We note that only one complete transverse oscillation of the coronal loop was clearly observed. Moreover, we also note that the jet oscillates in the transverse direction to its propagation (see Section 4).

Figure 1 shows that only half of the coronal loop is clearly visible. To enhance the contrast, we smoothed the images (to remove noise) and convolved them with the Laplacian operator to enhance the regions of the sharp change in brightness. The processed image is shown in the left panel of Figure 2. In order to estimate the length of the loop, we use the image obtained after the application of the Laplacian operator and choose ten points along the length of the loop. Then we interpolate a curve passing through these points using cubic spline fitting as shown in the right panel of Figure 2. This procedure is repeated several times to calculate the mean projected length L and the standard deviation of the coronal loop; which is estimated to be ∼ 377 Mm and 7 Mm, respectively. The length of the coronal

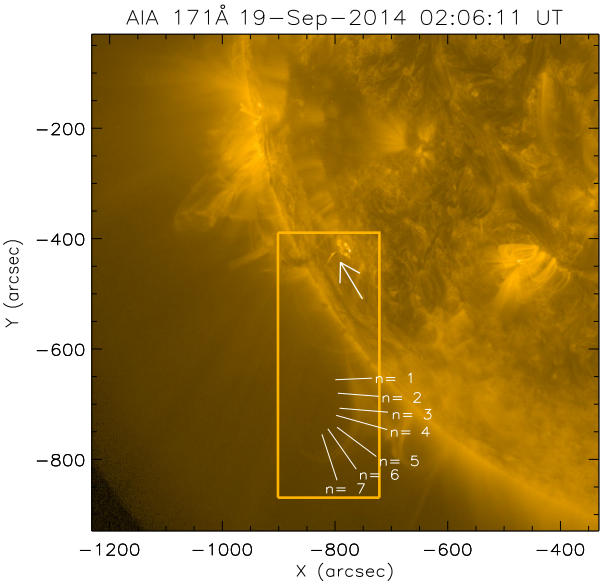

Figure 1 AIA/SDO image of 171 Å, taken on 19 September 2014 at 02:06:11 UT. The orange box highlights the jet (top) and the coronal loop (bottom). The white arrow points at the location of the jet. Seven artificial slices are placed perpendicular to different parts of the loop to detect the transverse oscillations (see Figure 3). An animation is available online as movie 1.

[1] http://sidc.oma.be/cactus/catalog/LASCO/2_5_0/2014/09/CME0080/CME.html.

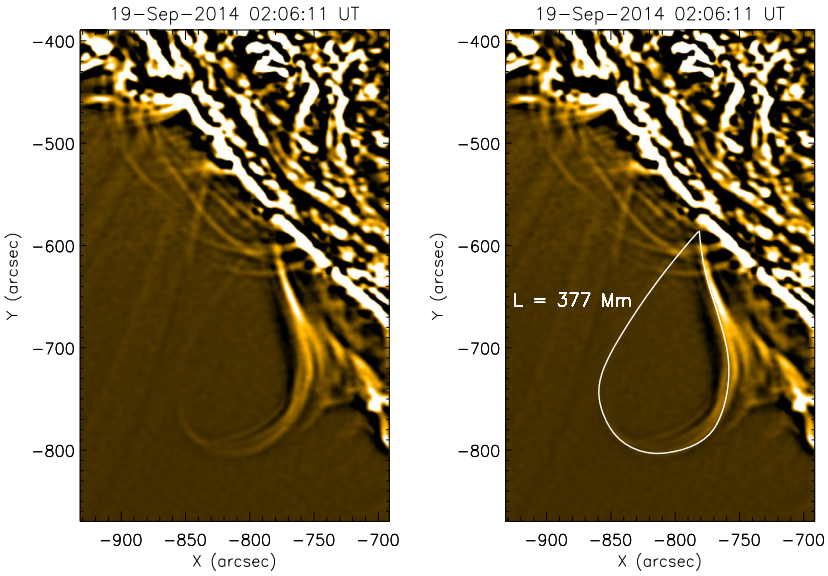

Figure 2 The left panel shows the coronal loop using feature enhancement by the Laplacian operator. The right panel shows the tracing of the loop, using cubic spline fitting.

loop estimated using this method can be taken as a lower limit of the loop length. Furthermore, we estimate the length of the loop assuming it to be a semicircle. We calculate the radius by estimating the distance between the solar limb and the coronal loop top. Since there is uncertainty in the estimation of the coronal loop top (because the coronal loop is quite thick), we take the thickness of the coronal loop as the error in the measurement of the radius. Using this, we estimate the length of the coronal loop to be 539 ± 30 Mm. This can be taken as the upper limit of the loop length. It is worth noting that the calculated radius is projected in the plane of sky. Thus the estimated length of the coronal loop still underestimates its true length.

2.1. Transverse Oscillations in the Coronal Loop

Seven artificial slices are placed perpendicular to the coronal loop to detect transverse oscillations. Corresponding to each slice, we generate a time–distance map, which is referred to as an x–t map throughout the manuscript. The x-axis represents time and the y-axis represents the distance along the slice.

Time–distance maps are sharpened using the unsharp mask technique. The sharpened maps are shown in Figure 3. It is quite evident from the x–t maps that the coronal loop undergoes transverse oscillations. It is also worth noting that the loop under study is not monolithic, but consists of many fine strands, which oscillate coherently.

To calculate the dynamic parameters for the coronal loop, first a Gaussian is fitted along each column of a given x–t map, and the mean values and one-sigma errors are estimated. We apply this procedure on the x–t maps for slices $n = 4, 5, 6$, and 7 only because slices $n = 1, 2$, and 3 are located near the footpoint of the coronal loop, thus the displacement of the coronal loop is very small. Moreover, near the footpoint of the coronal loop under study, there are many other fine loops along the line of sight that make the detection of transverse oscillation even more difficult. From the x–t maps, we note that the oscillations have a very

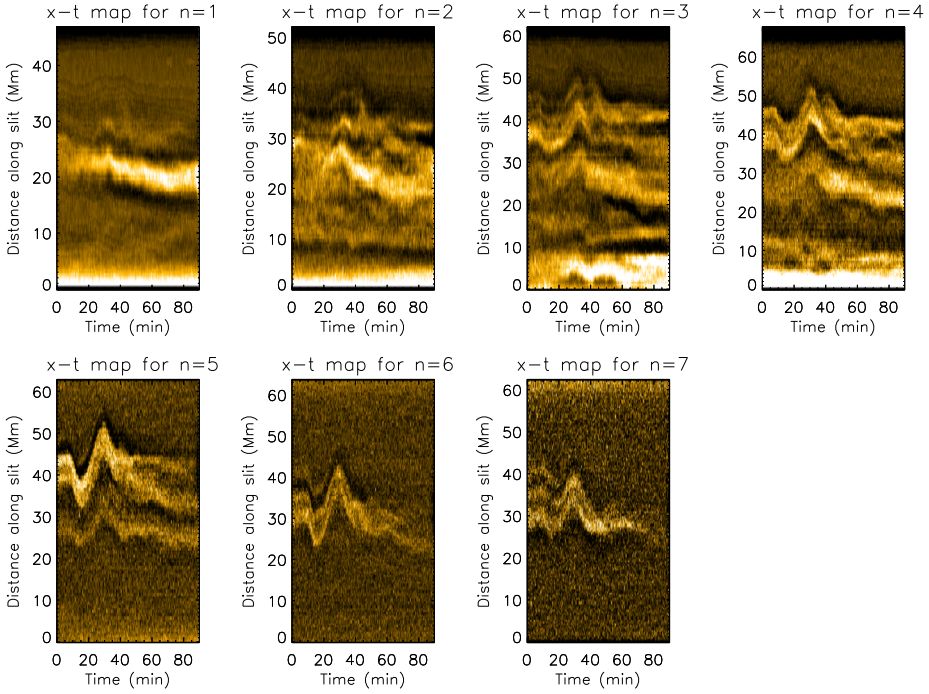

Figure 3 Sharpened x–t maps corresponding to the seven slices placed on the loop (see Figure 1). x–t maps were sharpened using an unsharp mask. The x–t graph shows the evidence of transverse oscillations in the coronal loop. We also note that the coronal loop is not monolithic, but a bundle of fine strands that oscillate coherently.

poor quality factor (only one complete cycle is observed with no clear gradual decrease of the amplitude), and therefore we fit the x–t maps with an undamped sinusoidal function having the expression

$$A(t) = C + A_0 \sin(\omega t + \phi), \tag{1}$$

where C is the equilibrium position of the loop, A_0 is the displacement amplitude, ω the oscillation frequency, and ϕ is the phase.

We use the MPFIT function (Markwardt, 2009) in the Interactive Data Language (IDL) to obtain the best-fit values of the undamped sinusoidal equation parameters. The best-fit sinusoidal curve with the best-fit parameters is shown in Figure 4.

From the fitted curves in Figure 4, we estimate the average oscillation period ($P = \frac{2\pi}{\omega}$) to be $\sim 32 \pm 5$ min. We note that oscillations at different positions along the coronal loop are in phase. This oscillation mode is called the global kink mode. We also note that the one footpoint of the loop appears to be anchored at the limb. Using the Laplacian filtered image (see Figure 2), we find that the other footpoint may be anchored behind the limb, thus we infer that this oscillation mode is the fundamental standing mode.

3. Observations Using STEREO

In this section, we use STEREO/EUVI-B 171, 195, and 304 Å images to obtain an additional perspective of the coronal loop and the jet. We explore whether it is possible to obtain a

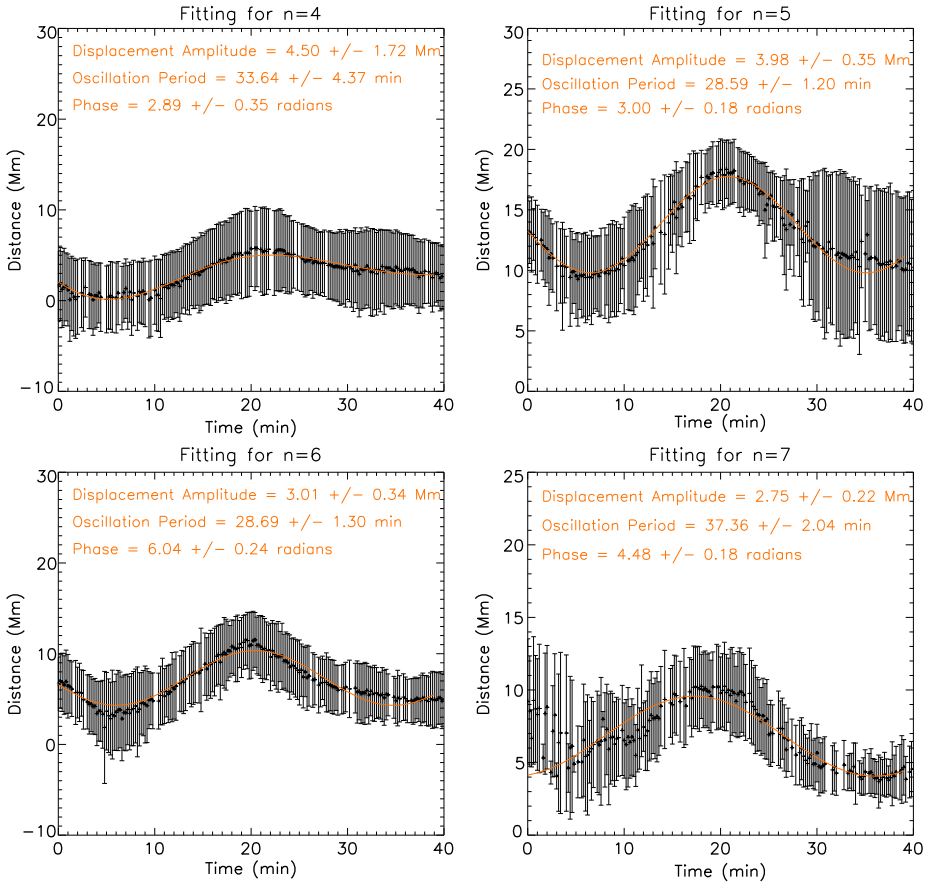

Figure 4 Best-fit sinusoidal curves with fitting parameters for four slices denoted by $n = 4, 5, 6$, and 7.

stereoscopic view of the loop and the jet. In Figure 5 the limb of the Sun as seen from AIA is overplotted on an EUVI 171 Å image, and the solar limb as seen from EUVI is overplotted on an AIA 171 Å image. We find that the jet source region is not observed in the EUVI 171 Å image because it is behind the limb. Since the cadence of EUVI 171 Å is one hour, we could not see the trajectory of the jet in EUVI 171 Å. In addition to this, only a few parts of the coronal loop under study are seen in EUVI 171 Å. The possible position of the loop under study is marked with a red arrow in EUVI 171 Å. The corresponding position in AIA 171 Å is also marked with a red arrow. We could not associate the loop features seen from EUVI 171 Å with the corresponding loop features seen from AIA 171 Å. For example, the loop we see in EUVI 171 Å (marked with a red arrow in EUVI 171 Å) could be the other footpoint of the coronal loop that is not clearly seen in the AIA 171 Å image (marked with a red arrow in AIA 171 Å). Thus it is extremely difficult to perform the triangulation in this scenario. We repeat the same analysis with EUVI 195 Å images (see Figure 6). Since EUVI 195 Å has a better cadence of 5 min, we are able to see the jet in one frame in EUVI 195. We have made a normal-intensity movie and a difference movie (movies 3 and 4) to illustrate it. Similarly, the jet is also seen in EUVI 304 Å difference images (see Figure 7). We have also made a

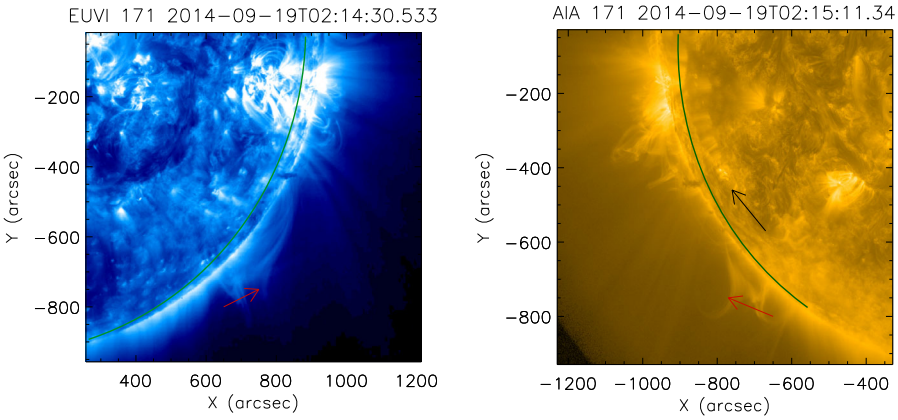

Figure 5 Left: STEREO/EUVI 171 Å image with the solar limb as seen from AIA 171 Å overplotted in green. The possible position of the loop corresponding to the loop seen in AIA 171 Å is marked with a red arrow. Right: SDO/AIA 171 Å image with the limb as seen from EUVI 171 Å overplotted in green. The loop under study is marked with a red arrow. The black arrow represents the location of the source region (footpoint) of the jet. Since the source region is behind the limb as seen from EUVI, it is not seen in the EUVI 171 Å image.

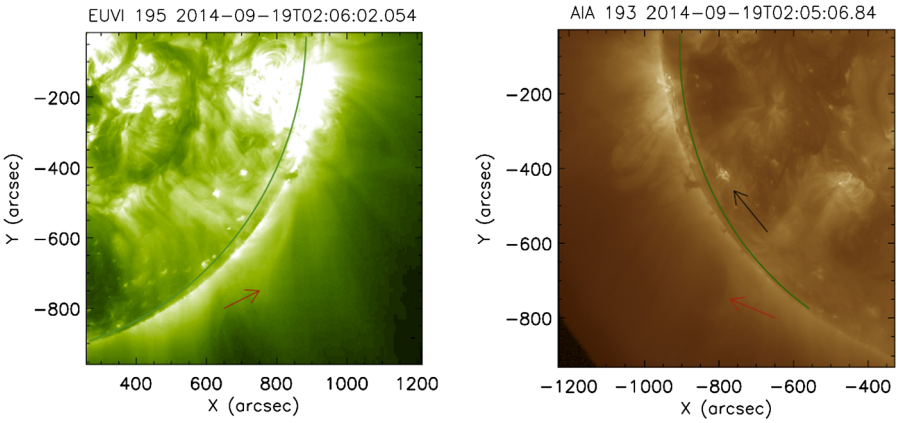

Figure 6 Left: STEREO/EUVI 195 Å image with the solar limb as seen from AIA 193 Å overplotted in green. Right: SDO/AIA 193 Å image with the limb as seen from EUVI 195 Å overplotted in green. The black arrow represents the location of the source region (footpoint) of the jet. Since the source region is behind the limb as seen from EUVI, it is not seen in the EUVI 195 Å image. The animations are available online as movies 3 and 4.

normal-intensity and a running-difference movie (movies 5 and 6) using EUVI 304 Å and AIA 304 Å.

3.1. EUVI 195 Å

In the difference movie of EUVI 195 Å and AIA 193 Å (movie 4), a disturbance is seen to be moving inward towards the solar disk in EUVI 195 Å. On close inspection of EUVI 195 Å images (see movie 3), we note that the plasma disappears at the location where we see a dark feature in difference images. It starts near the limb and propagates inward towards the disk

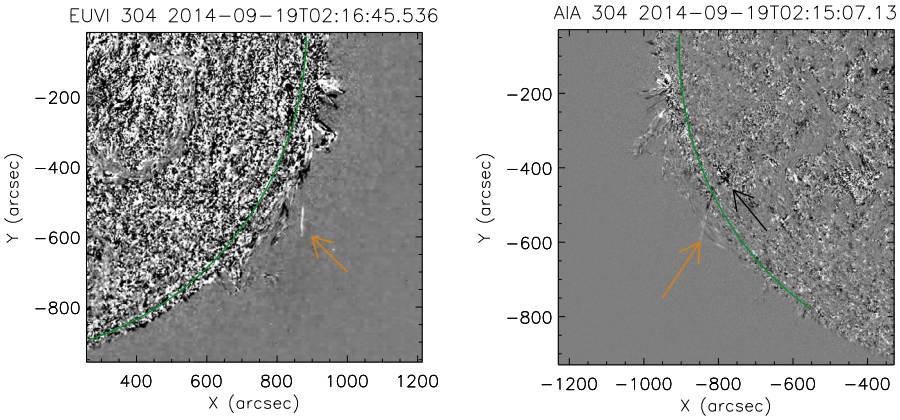

Figure 7 Left: STEREO/EUVI 304 Å difference image with the solar limb as seen from AIA 193 Å overplotted in green. Right: SDO/AIA 304 Å image with the limb as seen from EUVI 195 Å overplotted in green. The black arrow represents the location of the source region (footpoint) of jet. The orange arrow represents the jet in EUVI 304 Å and AIA 304 Å. The animations are available online as movies 5 and 6.

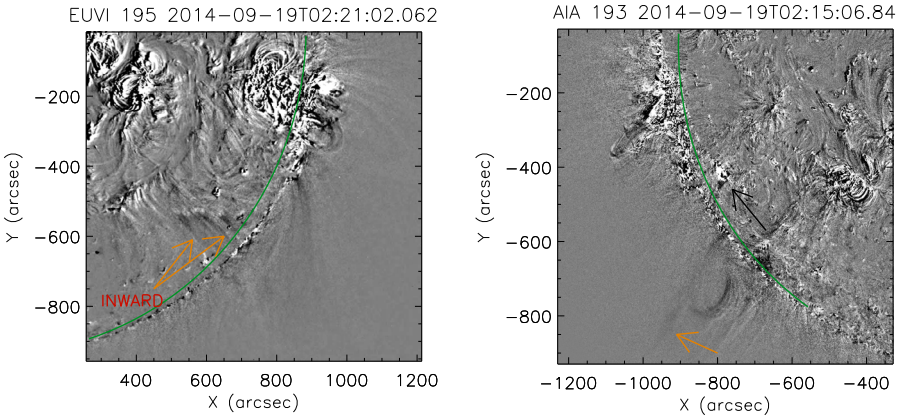

Figure 8 Left: STEREO/EUVI 195 Å difference image with the solar limb as seen from AIA 193 Å overplotted in green. Right: SDO/AIA 193 Å image with the limb as seen from EUVI 195 Å overplotted in green. The black arrow represents the location of the source region (footpoint) of the jet. The orange arrows represent the dark feature in EUVI 195 Å and AIA 193 Å.

(marked in Figure 8 (left panel)). This disappearance of plasma is visible as a dark feature in EUVI 195 Å difference images (see Figure 8). This is unlikely to be caused by an eruption because then it would have been propagating outward. Some scenarios might explain this: the disappearance may have been caused by the heating of the plasma from a nearby flare or some other event (a jet in this case) that transfers the energy to the surrounding medium. Secondly, a change in the magnetic field topology may have been brought about by magnetic reconnection, which might have caused plasma to escape through open field lines, which would appear as a dark feature in EUV 195 Å. Furthermore, it is also possible that the inward feature that is seen in EUVI-B 195 Å is the jet material falling down to the surface following the local magnetic field lines. We note from movie 4 that the dark feature first appears in AIA 193 Å. It interacts with the coronal loop and displaces it. Subsequently, it

appears in EUVI 195 Å and propagates inward. This means that the disturbance seen in EUVI 195 Å must be associated with the jet as seen in AIA.

4. Analysis of the Jet

High-resolution images obtained from AIA/SDO enable us to resolve the jet and characterise its properties. Jets are often observed near coronal holes (Chandrashekhar *et al.*, 2014). The appearance and dynamics of jets have been well studied because they contribute to coronal heating and solar wind acceleration (Chandrashekhar *et al.*, 2014; Mueller and Antiochos, 2008; Savcheva *et al.*, 2007; Shibata *et al.*, 1995).

The jet is seen in AIA 304 Å, 171 Å, 193 Å, 211 Å and to some extent in 94 Å. In AIA 304 Å and 171 Å the jet is seen as a bright collimated plasma propagating outward, while in hotter channels like AIA 211 Å and to some extent in 193 Å, we initially note bright collimated plasma, which becomes fainter at later times, followed by a dark emission that is most likely due to the heating of the plasma. In 94 Å we see a faint emission that suggests that the jet is multithermal in nature, having both cool and hot components (see movies 7 and 8). As explained above in AIA 211 Å and 193 Å, a dark feature seen in difference images is the manifestation of the dark emission seen in normal-intensity images. At the same location in AIA 94 Å a faint emission is seen that is the signature of heating (see Figure 9). The animations of difference images of AIA 211 Å and 94 Å are available online as movies 7 and 8, respectively. It is worth noting at this point that the dark feature seen in AIA 211 Å could either be the hot component of the jet, or it could be the signature of heating caused by the jet. However, the low signal-to-noise ratio prevented us from finding the bright emission in 94 Å, but a faint emission is clearly seen in the difference images. The heating mechanism is beyond the scope of the present study.

We found that the jet is associated with a B9 class flare as recorded by GOES-15, whose peak is recorded at 02:13 UT. It may also be possible that the inward-moving dark features observed with STEREO/EUVI-B 195 Å are the faint EUV wavefront triggered by the jet (Liu and Ofman, 2014) or that they are the result of jet material falling back to the solar

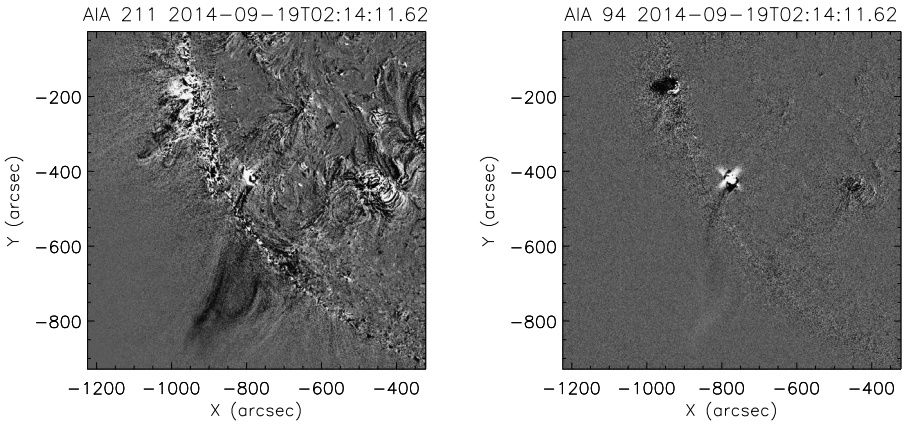

Figure 9 Left: SDO/AIA 211 Å difference image. A dark feature is visible near the loop. Right: SDO/AIA 94 Å image. A faint bright emission is visible near the loop. The animations are available online as movies 7 and 8.

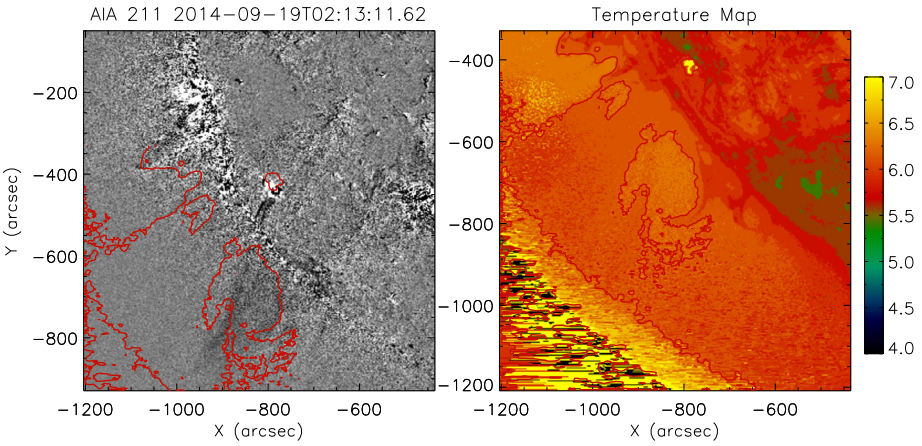

Figure 10 Left: SDO/AIA 211 Å difference image with contours of $\log(T) = 6.3$ ($\sim$2 MK) overplotted. Right: Temperature map (note the difference in field of view). The colour bar on the right represents $\log(T)$.

surface (Culhane *et al.*, 2007). We also estimate the temperature at the location of dark emission using the DEM technique developed by Aschwanden *et al.* (2013). We find at the location of dark emission seen in AIA 211 Å difference images that the temperature is hotter than in other regions. The right panel of Figure 10 shows the temperature map with contours of $\log(T) = 6.3$ overplotted, and the left panel shows the difference image of AIA 211 Å with contours of $\log(T) = 6.3$ overplotted in red. We note that the contours surround most of the dark emission seen in AIA 211 Å. We conjecture that the jet interacts with the loops, causing transverse oscillations, and it interacts with the ambient medium, transferring part of its energy and heating the local plasma. This heating causes plasma to disappear from the AIA 193 and 211 Å passbands, thus dark features appear in the hotter channel. When this heating shifts towards the far side, beyond the limb, we see it as a dark feature propagating inward in EUVI 195 Å. Moreover, as pointed out in Section 3.1, the propagating dark feature seen in EUVI 195 Å could be the jet plasma falling back towards the Sun.

We estimate the velocity of the jet by creating an x–t map. To generate the x–t map, we isolate the trajectory of the jet. We choose a few points along the path through which the jet propagates (starting from the time of jet eruption until the jet vanishes). Next, we interpolate a curve between these points using cubic spline fitting. We plot another curve, 50 pixels apart, parallel to it, so that the jet propagates within the region outlined by the two white curves as shown in the left hand panel of Figure 11, in spite of the transverse displacement of the jet. The trajectory of the jet, marked with white curves, is shown in a movie available online (see movie 2). Finally, we average the intensity between the two curves and create the x–t map. The x–t map is shown in the right panel of Figure 11. The inclined ridge in the x–t map represents the jet propagating outward along the chosen curved artificial slice. We fit a straight line by eye. The velocity of the jet is estimated by calculating the slope of the fitted line, which is found to be $\sim 43 \pm 4$ km s^{-1}. We use the same analysis in the AIA 211 Å difference images and generate x–t map as shown in Figure 12. In this case, we choose a broad straight slice to ensure that both bright and dark features remain within the slit for the entire duration of the analysis. In the right panel of Figure 12, we see bright and dark ridges. The bright ridge corresponds to jet material and is estimated to be propagating with a speed of 63 km s^{-1}. The dark emission is estimated to be propagating with a speed of 168 km s^{-1}. This could either be the hot component of jet or the heating caused by jet eruption, which is

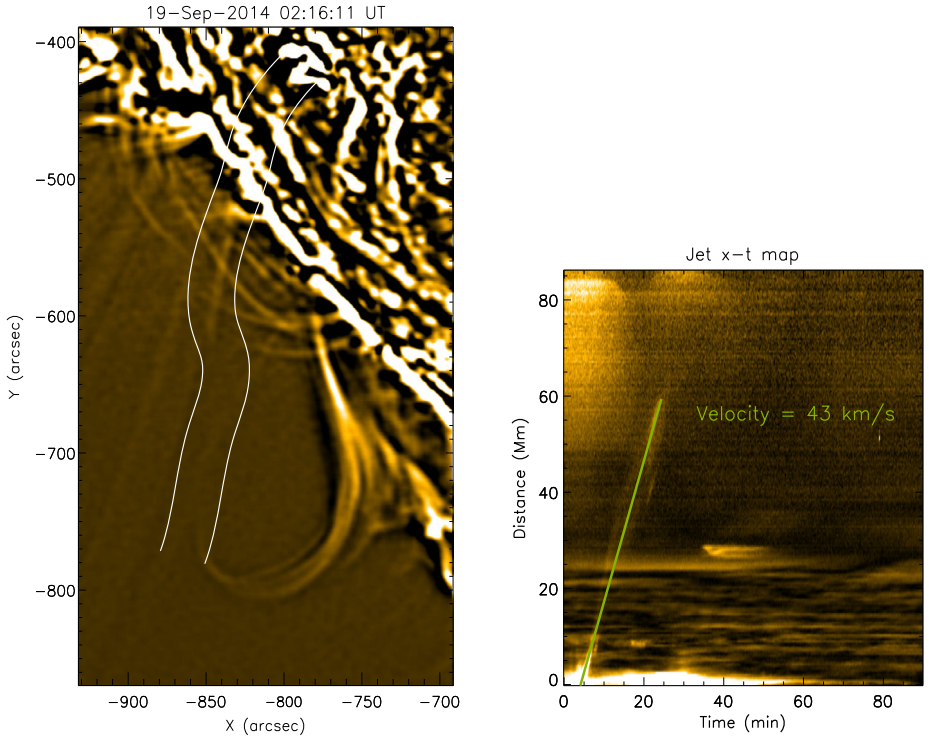

Figure 11 The left panel shows the region of jet propagation outlined by two parallel curves. The right panel represents the x–t map for the selected region (shown in the left panel). The fitted straight line is shown in green. The jet velocity is found to be $\sim 43 \pm 4$ km s^{-1}. An animation is available online as movie 2.

propagating outward. However, the low signal-to-noise ratio in AIA 94 Å prevented us from making x–t maps of AIA 94 Å.

We also analyse the transverse oscillations in the jet as it propagates. Since the jet propagates while it oscillates, we place 40 artificial slices along the jet propagation axis to capture the transverse oscillations. This is done by joining 40 equidistant points of one of the curves to their corresponding parallel points at the other curve. This produces 40 transverse slits at 40 equidistant positions along the jet axis, as shown in Figure 13.

We create x–t maps for individual slices and add them. The resulting x–t map is shown in Figure 14. Since the jet becomes fainter as it propagates outward, the jet intensity decreases with time in the x–t maps. We find that high and low periodicities are co-existent. The high-frequency signal is only present in a region close to the footpoint of the jet, however. We fit two sinusoidal curves in Figure 14 shown as white and green curves, and find a periodicity of 2 min and 24 min, respectively. It is important to note that the time period of the jet oscillation ($\sim$24 min) is nearly equal to the time period of the coronal loop oscillations ($\sim$31 min).

5. MHD Seismology

We assume the coronal loop to be a cylindrical magnetic flux tube of uniform magnetic field B_0, where the minor radius a, that is, the half-width of the coronal loop cross-section,

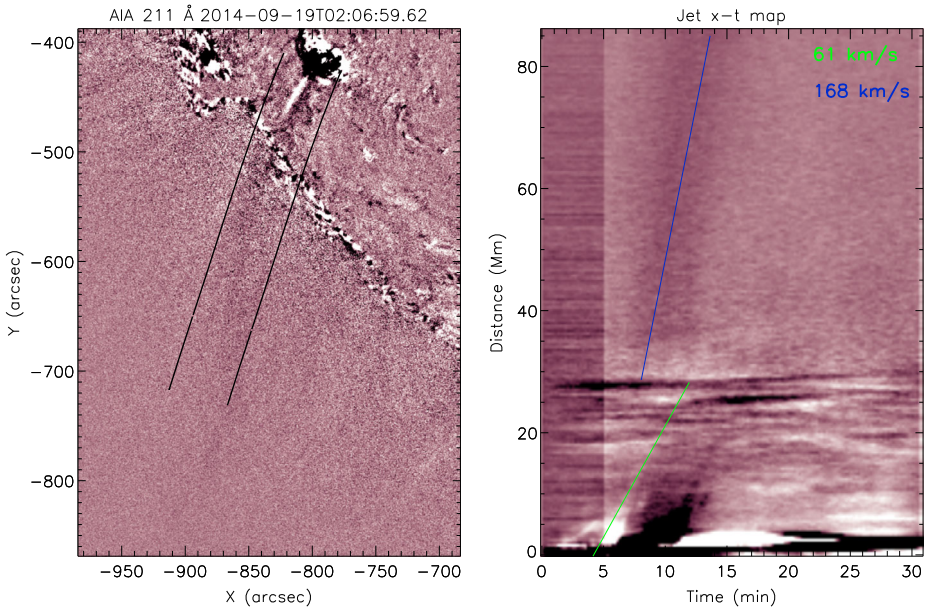

Figure 12 Left: SDO/AIA 211 Å difference image. The jet trajectory is outlined by two parallel lines. Right: x–t map for the selected region (shown in the left panel). Two features, a bright and a dark ridge, are fitted with green and blue lines, respectively.

is $\ll L$ (where L is the total length of the loop). This is called the thin-tube (TT) or long-wavelength approximation. Thus, $k_z a \ll 1$ (where $k_z = 2\pi/\lambda$ and $\lambda = 2L$ for the fundamental mode). In TT approximation, the phase speed $V_{\rm ph}$ is the same as the kink speed $C_{\rm K}$ (Nakariakov and Verwichte, 2005):

$$V_{\rm ph} = C_{\rm K} = \frac{2L}{P}, \tag{2}$$

where $C_{\rm K}$ is also defined as the density-averaged Alfvén speed, *i.e.*

$$C_{\rm K} = \sqrt{\frac{\rho_0 C_{A0}^2 + \rho_e C_{Ae}^2}{\rho_0 + \rho_e}}, \tag{3}$$

where ρ_0 and ρ_e are the density of uniform plasma inside and outside the loop, respectively, and C_{A0} and C_{Ae} are the internal and external Alfvén speeds, which can be defined as

$$C_{A0} = B_0/\sqrt{\mu_0 \rho_0}, \tag{4}$$

$$C_{Ae} = B_e/\sqrt{\mu_0 \rho_e}, \tag{5}$$

where B_0 and B_e are the internal and external magnetic fields, respectively, for the coronal loop.

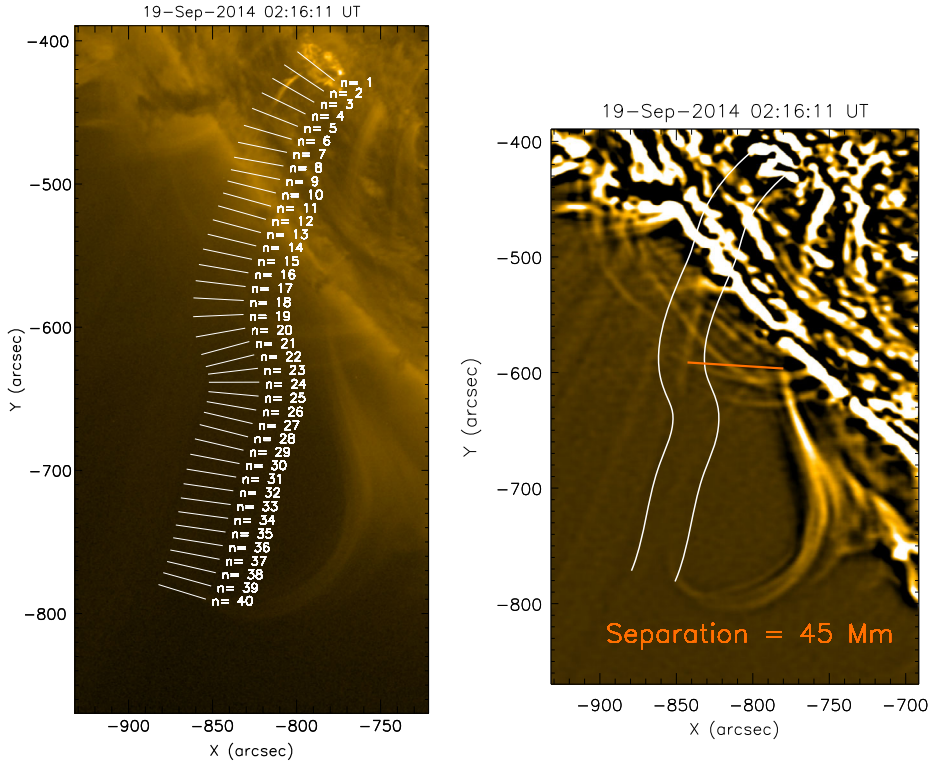

Figure 13 Left: the figure shows 40 transverse slits at 40 equidistant points along the jet propagation axis. Right: figure showing the separation between the oscillating jet and the coronal loop.

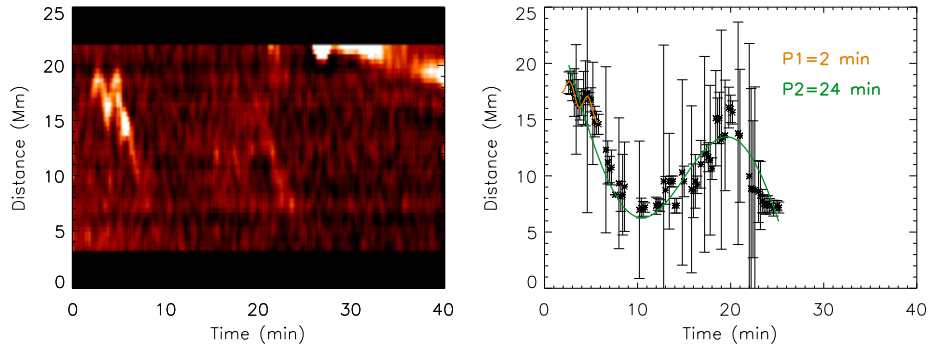

Figure 14 Left: x–t map obtained after adding all artificial slices as shown in Figure 13. Right: orange and green curves represent the best-fit sinusoidal curves. Corresponding periods are mentioned in the figure.

Substituting Equations (4) and (5) into Equation (3), and assuming that the internal and external magnetic fields of the loop are equal, we obtain

$$C_{A0} = \frac{C_K}{\sqrt{\frac{2}{1+\frac{\rho_e}{\rho_0}}}}. \tag{6}$$

Table 1 Estimation of the Alfvén speed and the magnetic field strength inside the coronal loop.

$\frac{\rho_e}{\rho_0}$	Projected length			Semicircular model		
	0.1	0.4	0.7	0.1	0.4	0.7
C_{A0} (km s^{-1})	299 ± 27	328 ± 14	361 ± 16	415 ± 28	469 ± 32	516 ± 35
B (G)	2.68 ± 0.64	2.86 ± 0.12	3.20 ± 0.14	3.62 ± 0.24	4.1 ± 0.28	4.5 ± 0.31

Using Equation (2), we estimate the kink speed ($C_{\rm K}$) to be $\sim 392 \pm 17$ km s^{-1} (and $\sim 560 \pm 38$ km s^{-1}, assuming coronal loop to be semicircle) and the internal Alfvén velocity $\sim 299 \pm 27$ km s^{-1} (and $\sim 415 \pm 28$ km s^{-1}, assuming the coronal loop to be a semicircle), assuming a density contrast ($\frac{\rho_e}{\rho_0}$) = 0.1. It is worth noting at this point that the density contrast depends on the EUV intensity ratio as $(\frac{\rho_e}{\rho_0})^2 = \frac{I_e}{I_o}$, where I_e and I_o are EUV intensity of the background and inside the loop, respectively. We find that the intensity ratio along the loop changes from loop footpoint to the loop top. Furthermore, we also note that the intensity ratio at a given position along the coronal loop changes as it oscillates, presumably as a result of variations in the column depth of the loop along the line of sight by the wave (Cooper, Nakariakov, and Tsiklauri, 2003). We estimate the intensity ratio at several places along the loop and at different times. We find that the intensity ratio varies from 0.18 to 0.5. Thus the density contrast varies from 0.4 to 0.7. We use AIA 171 Å for the analysis because the loop is best visible in this wavelength. However, it is important to note that the intensity contrast of the loop also depends on its orientation, thus the density contrast may still be a rough estimate. Table 1 shows the estimation of the Alfvén speed and the magnetic field strength for different values of the density contrast (*i.e.* 0.1, 0.4, and 0.7). We keep 0.1 for comparison since this is a typical value which is used in most studies. Using Equation (4) and taking $\mu_0 = 4\pi \times 10^{-7}$ H m^{-1} (in SI units), we can estimate the magnetic field inside the coronal loop (B_0), provided the internal density of the coronal loop is known.

5.1. Density Estimate Using DEM Analysis

To calculate the internal density of the coronal loop, we use the differential emission measure (DEM) analysis technique developed by Aschwanden *et al.* (2013). Using this automated technique, we obtain that the number density of the electrons (n_e) is $10^{8.56\pm0.17}$ cm^{-3} and the average temperature is $10^{5.79\pm0.21}$ K (see Figure 15).

5.2. Calculation of the Magnetic Field Inside the Coronal Loop

Estimating the electron density using DEM and assuming H:He = 10:1, we obtain the magnetic field strength inside the coronal loop for different values of the density contrast using Equations (4) and (6) (see Table 1). The estimated value of the magnetic field inside the loop is lower than in active-region loops.

6. Energy Estimates

To understand whether the jet can trigger the transverse oscillations in the coronal loop, we calculate the energy density of the jet and compare it with the energy density of the oscillating coronal loop. Although both transverse oscillations and linear motion contribute

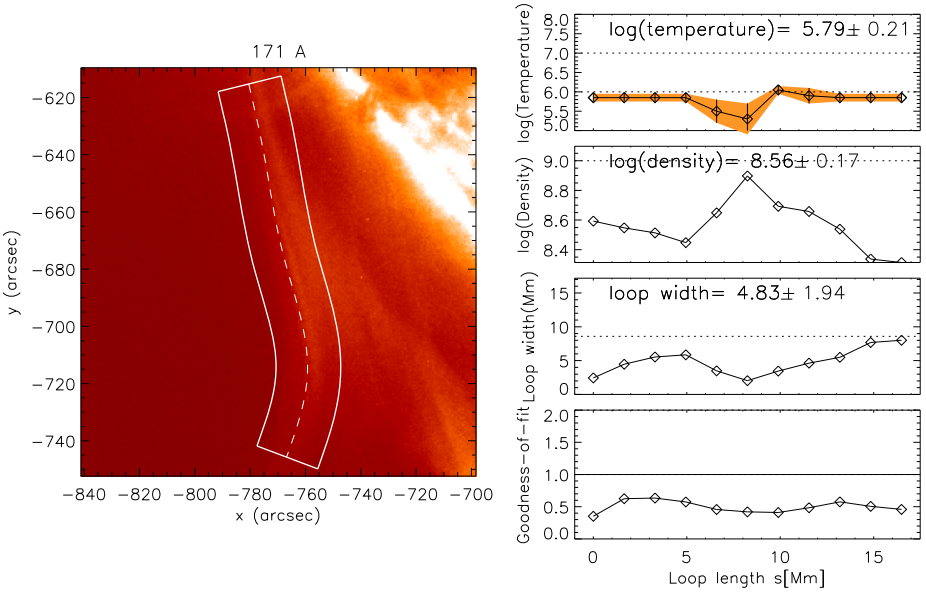

Figure 15 The left panel shows the location of the loop, enclosed in curves, that we selected for analysis. The best-fit values of the DEM peak temperature, the electron densities, loop widths, and the goodness-of-fit χ^2 for the 171 Å Gaussian DEM fits are shown in the right panel of the graph.

to the energy density of the jet, we estimate energy density of the jet due to only linear motion. Moreover, we estimate energy density using the bright feature of the jet. We do not consider the energy density of the hot jet component since it is very difficult to measure its density and thus its energy density. Therefore, it should be borne in mind that the energy density of the jet is an underestimate of the total energy density. The energy density of the propagating jet due to its linear motion is defined as

$$E_{\rm jet} = \tfrac{1}{2}\rho_{\rm jet} v^2, \tag{7}$$

where $\rho_{\rm jet}$ is the density of the jet. The typical value of the number density of the jet is reported to be between 10^9 cm^{-3} (Shimojo and Shibata, 2000) to 10^{10} cm^{-3} (Madjarska, 2011; Moreno-Insertis and Galsgaard, 2013).

We also estimate the number density of the jet using DEM at the instant when it is clearly observed. The density is estimated to be $10^{9.92}$ cm^{-3}. v is the velocity of the jet, which is found to be $\sim 43 \pm 4$ km s^{-1} (see Section 4). Using $n_{\rm jet} = 10^{10}$ cm^{-3} and the jet velocity, we estimate the energy density to be $(19.6 \pm 3.6) \times 10^{-3}$ J m^{-3}.

The energy density of the oscillating loop is defined as (Goossens *et al.*, 2013)

$$E_{\rm monolithic} = \tfrac{1}{4}\rho_0 \omega^2 {A_0}^2, \tag{8}$$

where ρ_0 is the internal density of the coronal loop. Using DEM, we estimate the number density inside the loop to be $10^{8.56\pm0.17}$ cm^{-3}. ω is the angular frequency of the oscillating loop ($\omega = kC_{\rm K} = \frac{\pi}{L}C_{\rm K}$, where $k = \frac{2\pi}{\lambda}$ and $\lambda = 2L$ for the fundamental vibration mode). Thus, $\omega = (3.36 \pm 0.36) \times 10^{-3}$ s^{-1} (and $3.27 \pm 0.19 \times 10^{-3}$ s^{-1} assuming the loop to be a semicircle) using the parameters estimated in Section 5.2. A_0 is the displacement amplitude.

The displacement amplitude for $n = 4$ slice is $\sim 4.50 \pm 1.72$ Mm, which is the largest of all the slices (see Figure 4). We estimate that the energy density of the loop corresponding to this amplitude is $\sim (3.28 \pm 0.89) \times 10^{-5}$ J m^{-3} ($\sim (3.26 \pm 0.23) \times 10^{-5}$ J m^{-3} assuming the loop to be a semicircle). For $n = 7$ slice, the displacement amplitude is $\sim 2.75 \pm 0.22$ Mm, which is the smallest of all the slices, the energy density is estimated to be $\sim (1.23 \pm 0.09) \times 10^{-5}$ J m^{-3} ($\sim (1.22 \pm 0.1) \times 10^{-5}$ J m^{-3} assuming the loop to be a semicircle). Therefore, the energy density of the oscillating loop is within the range of $(1.22 - 3.28) \times 10^{-5}$ J m^{-3}.

Since the coronal loop is not monolithic and consists of many fine loops, we estimate the energy density using a multistranded loop model. The energy density in the multistranded oscillating coronal loop is given by

$$E_{\text{multistrand}} = \tfrac{1}{2} f (\rho_0 + \rho_e) \omega^2 {A_0}^2, \tag{9}$$

where ρ_e is the external density of the coronal loop. f is the filling factor, which is defined as the ratio of the sum of the volume of an individual flux tube ensemble together with the total volume containing flux tubes. Using Equations (8) and (9), we obtain

$$\frac{E_{\text{multistrand}}}{E_{\text{monolithic}}} = 2f \left(1 + \frac{\rho_e}{\rho_o} \right). \tag{10}$$

We calculate the filling factor, f, as defined above at several instances along the length of coronal loop. The mean and standard deviations are estimated. Therefore, f is found to be 0.17 ± 0.03. Substituting the value of f in Equation (10), we find that $E_{\text{multistrand}} = 0.434\ E_{\text{monolithic}}$ for the density contrast of 0.1. $E_{\text{multistrand}} = 0.476\ E_{\text{monolithic}}$ and $E_{\text{multistrand}} = 0.578\ E_{\text{monolithic}}$ assuming the density contrasts to be 0.4 and 0.7, respectively. Therefore, we find that the energy density of the jet is much greater than the energy density of the coronal loop. The jet might be transferring a part of its energy to displace the loop. Hence, the jet can be inferred to be the cause of the transverse oscillations in the coronal loop.

7. Interaction Between Jet and Loop

In Section 6 we found that the jet has enough energy to excite oscillations in the coronal loop. In running difference movies of AIA 211 Å (see movie 7) we find evidence of hot and cool components of a jet that hits the coronal loop. This could be a simple projection effect, but we do not know which trajectory the jet follows: maybe it curves, hits the loops, and some part of the jet plasma is seen as the inward-moving feature in STEREO/EUVI 195 Å.

Furthermore, a collective transverse oscillation in two flux tubes is also possible. The magnetic field of the jet spine constitutes a flux tube that includes flowing plasma and is subject to long-period (24 min) transverse oscillations. The coronal loop is another flux tube that originally is in equilibrium in the vicinity of the jet plasma column. The separation between the oscillating jet and the coronal loop is estimated to be ~ 45 Mm, as shown in Figure 13 (right panel). Luna *et al.* (2008) studied the collective kink oscillations of two identical parallel magnetic flux tubes. They found that there are four oscillation modes in such a system in which two are in-phase oscillations. Later, Van Doorsselaere, Ruderman, and Robertson (2008) reported that the kink oscillations of the system of two non-identical tubes is degenerate. They found that similarly to the kink oscillations of a single tube with circular cross-section, there is no preferable direction of the kink oscillation polarization, and the two long-period (and also short-period) oscillations merge with each other to form two oscillatory modes (one with a long period, and another with a short period).

Significant developments have also been made considering the various models demonstrating the damping of the kink oscillations in multiple magnetic fluxtubes (Luna *et al.*, 2009, 2010; Ofman, 2009; Terradas *et al.*, 2008). The linear theory of the resonant damping of kink oscillations in two parallel magnetic tubes is also developed by Robertson and Ruderman (2011). It should be noted that the observed jet shows transverse kink oscillations of two periods: 21 min (long) and 2 min (short) (Figure 14). The loop in the vicinity also exhibits similar transverse oscillations, although only a long period (31 min) is detectable in the observational base line. Moreover, the long-period kink waves in both flux systems are almost out of phase. It should be borne in mind that we do not know that at which location and time the jet interacts with the loop. It may not be necessary that the visible jet material has to strike the loop. Both the jet and coronal loop are magnetic flux tubes, thus the interaction between them may occur earlier than the observational signatures it produces. If the jet interacted with the loop and triggered oscillations before the bright visible material reached the same location, in that scenario, at the instant when bright material will appear adjacent to coronal loop, both systems might go out of phase. Both flux tubes, *i.e.*, the upper magnetoplasma column of the jet and the part of the coronal loop in its vicinity (45 Mm apart), are non-identical flux tubes as their plasma and magnetic field properties are essentially not the same. It is worth noting at this point that this distance is projected in the plane of sky and therefore is an underestimate of the real distance, which could be higher. Therefore, the model of Van Doorsselaere, Ruderman, and Robertson (2008) might be at work in the present observational base-line where the transverse oscillations of the short period (2.0 min) and the long period (21 min) both are excited in the jet (Figure 14). The two modes with the longer period are most likely merged in one degenerate mode, and the same occurred with the two modes with the shorter period. Since the modes from each pair are polarized in the mutually orthogonal directions (*cf.* Figure 14), the degenerate modes created by merging of two modes can be arbitrarily polarized. The long-period mode is only detected in the coronal loop, while the short period is not detected. The reason may be that the plane-of-loop apex is in such an orientation that the arbitrarily set polarization direction of the short-period oscillations (which is seen in the jet body) is non-identifiable.

8. Conclusions

We reported large amplitude and long-period transverse oscillations in a coronal loop that have most likely been triggered by a nearby oscillating jet. We find that the jet appears as a bright feature in all AIA channels, but soon disappears from hot channels like 211 Å. A faint emission is also seen in AIA 211 Å, which is considered a signature of heating. We estimated the length of the loop by two different methods. (i) Calculating the projected distance of the loop in the plane of sky, which can be considered as the lower limit of the loop length, and (ii) estimating the loop length by assuming a semicircular geometry, which can be considered as the upper limit of the length of the loop. Based on this, we estimate the lower (upper) limit of the kink speed and the Alfvén speed to be $\sim 392 \pm 17$ (560 ± 38) $\mathrm{km\,s^{-1}}$ and $\sim 299 \pm 27$ (516 ± 35) $\mathrm{km\,s^{-1}}$. We used the seismic inversion technique to estimate the magnetic field strength inside the coronal loop. We estimate the lower (upper) limit of the strength of the magnetic field inside coronal loop to be $\sim 2.68 \pm 0.64$ (4.5 ± 0.31) G, which is lower than a typical value of the magnetic field inside a coronal loop. The reason might be that it is not an active-region coronal loop. Finally, we estimated the energy density of loop. We find that the energy density varies from 1.22×10^{-5} $\mathrm{J\,m^{-3}}$ to 3.28×10^{-5} $\mathrm{J\,m^{-3}}$, which is about two to three orders of magnitude lower than the energy

density of the jet ($\sim (19.6 \pm 3.6) \times 10^{-3}$ J m^{-3}). We therefore conclude that the energy stored in the jet is found to be enough to excite oscillations in the coronal loop. The present observations also support the model of the collective transverse oscillations of two non-identical magnetic flux tubes in which long- and short-period modes are excited with an arbitrary polarization direction (Van Doorsselaere, Ruderman, and Robertson, 2008).

Acknowledgements We thank M. Ruderman for fruitful discussions. We also thank the anonymous referee for the useful suggestions that have enabled us to substantially improve the content of the manuscript.

Disclosure of Potential Conflicts of Interest The authors declare that they have no conflicts of interest.

References

Anfinogentov, S.A., Nakariakov, V.M., Nisticò, G.: 2015, Decayless low-amplitude kink oscillations: A common phenomenon in the solar corona? *Astron. Astrophys.* **583**, A136. DOI. ADS.

Aschwanden, M.J.: 2006, Coronal magnetohydrodynamic waves and oscillations: Observations and quests. *Phil. Trans. Roy. Soc. London Ser. A, Math. Phys. Sci.* **364**, 417. DOI. ADS.

Aschwanden, M.J., Schrijver, C.J.: 2011, Coronal loop oscillations observed with atmospheric imaging assembly – Kink mode with cross-sectional and density oscillations. *Astrophys. J.* **736**, 102. DOI. ADS.

Aschwanden, M.J., Fletcher, L., Schrijver, C.J., Alexander, D.: 1999, Coronal loop oscillations observed with the transition region and coronal explorer. *Astrophys. J.* **520**, 880. DOI. ADS.

Aschwanden, M.J., de Pontieu, B., Schrijver, C.J., Title, A.M.: 2002, Transverse oscillations in coronal loops observed with TRACE II. Measurements of geometric and physical parameters. *Solar Phys.* **206**, 99. DOI. ADS.

Aschwanden, M.J., Boerner, P., Schrijver, C.J., Malanushenko, A.: 2013, Automated temperature and emission measure analysis of coronal loops and active regions observed with the atmospheric imaging assembly on the solar dynamics observatory (SDO/AIA). *Solar Phys.* **283**, 5. DOI. ADS.

Chandrashekhar, K., Bemporad, A., Banerjee, D., Gupta, G.R., Teriaca, L.: 2014, Characteristics of polar coronal hole jets. *Astron. Astrophys.* **561**, A104. DOI. ADS.

Cooper, F.C., Nakariakov, V.M., Tsiklauri, D.: 2003, Line-of-sight effects on observability of kink and sausage modes in coronal structures with imaging telescopes. *Astron. Astrophys.* **397**, 765. DOI. ADS.

Culhane, L., Harra, L.K., Baker, D., van Driel-Gesztelyi, L., Sun, J., Doschek, G.A., Brooks, D.H., Lundquist, L.L., Kamio, S., Young, P.R., Hansteen, V.H.: 2007, Hinode EUV study of jets in the Sun's South polar corona. *Publ. Astron. Soc. Japan* **59**, S751. DOI. ADS.

Edwin, P.M., Roberts, B.: 1983, Wave propagation in a magnetic cylinder. *Solar Phys.* **88**, 179. DOI. ADS.

Feng, L., Inhester, B., de Patoul, J., Wiegelmann, T., Gan, W.Q.: 2012, Particle kinetic analysis of a polar jet from SECCHI COR data. *Astron. Astrophys.* **538**, A34. DOI. ADS.

Goossens, M., Andries, J., Aschwanden, M.J.: 2002, Coronal loop oscillations. An interpretation in terms of resonant absorption of quasi-mode kink oscillations. *Astron. Astrophys.* **394**, L39. DOI. ADS.

Goossens, M., Van Doorsselaere, T., Soler, R., Verth, G.: 2013, Energy content and propagation in transverse solar atmospheric waves. *Astrophys. J.* **768**, 191. DOI. ADS.

Hollweg, J.V., Yang, G.: 1988, Resonance absorption of compressible magnetohydrodynamic waves at thin 'surfaces'. *J. Geophys. Res.* **93**, 5423. DOI. ADS.

Hori, K., Ichimoto, K., Sakurai, T., Sano, I., Nishino, Y.: 2005, Flare-associated coronal disturbances observed with the norikura green-line imaging system. I. A coronal mass ejection onset. *Astrophys. J.* **618**, 1001. DOI. ADS.

Lee, J., White, S.M., Kundu, M.R., Mikić, Z., McClymont, A.N.: 1999, A test for coronal magnetic field extrapolations. *Astrophys. J.* **510**, 413. DOI. ADS.

Lemen, J.R., Title, A.M., Akin, D.J., Boerner, P.F., Chou, C., Drake, J.F., Duncan, D.W., Edwards, C.G., Friedlaender, F.M., Heyman, G.F., Hurlburt, N.E., Katz, N.L., Kushner, G.D., Levay, M., Lindgren, R.W., Mathur, D.P., McFeaters, E.L., Mitchell, S., Rehse, R.A., Schrijver, C.J., Springer, L.A., Stern, R.A., Tarbell, T.D., Wuelser, J.-P., Wolfson, C.J., Yanari, C., Bookbinder, J.A., Cheimets, P.N., Caldwell, D., Deluca, E.E., Gates, R., Golub, L., Park, S., Podgorski, W.A., Bush, R.I., Scherrer, P.H., Gummin, M.A., Smith, P., Auker, G., Jerram, P., Pool, P., Soufli, R., Windt, D.L., Beardsley, S., Clapp, M., Lang, J., Waltham, N.: 2012, The Atmospheric Imaging Assembly (AIA) on the Solar Dynamics Observatory (SDO). *Solar Phys.* **275**, 17. DOI. ADS.

Liu, W., Ofman, L.: 2014, Advances in observing various coronal EUV waves in the SDO era and their seismological applications (invited review). *Solar Phys.* **289**, 3233. DOI. ADS.

Luna, M., Terradas, J., Oliver, R., Ballester, J.L.: 2008, Transverse oscillations of two coronal loops. *Astrophys. J.* **676**, 717. DOI. ADS.
Luna, M., Terradas, J., Oliver, R., Ballester, J.L.: 2009, Transverse oscillations of systems of coronal loops. *Astrophys. J.* **692**, 1582. DOI. ADS.
Luna, M., Terradas, J., Oliver, R., Ballester, J.L.: 2010, Transverse oscillations of a multi-stranded loop. *Astrophys. J.* **716**, 1371. DOI. ADS.
Madjarska, M.S.: 2011, Dynamics and plasma properties of an X-ray jet from SUMER, EIS, XRT, and EUVI A & B simultaneous observations. *Astron. Astrophys.* **526**, A19. DOI. ADS.
Markwardt, C.B.: 2009, Non-linear least-squares fitting in IDL with MPFIT. In: Bohlender, D.A., Durand, D., Dowler, P. (eds.) *Astronomical Data Analysis Software and Systems XVIII*, *Astron. Soc. Pac. Conf. Ser.* **411**, 251. ADS.
Mathioudakis, M., Jess, D.B., Erdélyi, R.: 2013, Alfvén waves in the solar atmosphere. From theory to observations. *Space Sci. Rev.* **175**, 1. DOI. ADS.
Moreno-Insertis, F., Galsgaard, K.: 2013, Plasma jets and eruptions in solar coronal holes: A three-dimensional flux emergence experiment. *Astrophys. J.* **771**, 20. DOI. ADS.
Mueller, D.A.N., Antiochos, S.K.: 2008, A mechanism for coronal hole jets. *Ann. Geophys.* **26**, 1. DOI.
Nakariakov, V.M.: 2000, Flare-generated coronal loop oscillations: A tool for MHD coronal seismology. In: Verheest, F., Goossens, M., Hellberg, M.A., Bharuthram, R. (eds.) *Waves in Dusty, Solar, and Space Plasmas*, *Am. Inst. Phys. Conf. Ser.* **537**, 264. DOI. ADS.
Nakariakov, V.M., Ofman, L.: 2001, Determination of the coronal magnetic field by coronal loop oscillations. *Astron. Astrophys.* **372**, L53. DOI. ADS.
Nakariakov, V.M., Verwichte, E.: 2005, Coronal waves and oscillations. *Living Rev. Solar Phys.* **2**, 3. DOI. ADS.
Nakariakov, V.M., Ofman, L., Deluca, E.E., Roberts, B., Davila, J.M.: 1999, TRACE observation of damped coronal loop oscillations: Implications for coronal heating. *Science* **285**, 862. DOI. ADS.
Nisticò, G., Nakariakov, V.M., Verwichte, E.: 2013, Decaying and decayless transverse oscillations of a coronal loop. *Astron. Astrophys.* **552**, A57. DOI. ADS.
Nisticò, G., Bothmer, V., Patsourakos, S., Zimbardo, G.: 2009, Characteristics of EUV coronal jets observed with STEREO/SECCHI. *Solar Phys.* **259**, 87. DOI. ADS.
Ofman, L.: 2009, Three-dimensional magnetohydrodynamic models of twisted multithreaded coronal loop oscillations. *Astrophys. J.* **694**, 502. DOI. ADS.
Ofman, L., Wang, T.: 2002, Hot coronal loop oscillations observed by SUMER: Slow magnetosonic wave damping by thermal conduction. *Astrophys. J. Lett.* **580**, L85. DOI. ADS.
O'Shea, E., Srivastava, A.K., Doyle, J.G., Banerjee, D.: 2007, Evidence for wave harmonics in cool loops. *Astron. Astrophys.* **473**, L13. DOI. ADS.
Paraschiv, A.R., Lacatus, D.A., Badescu, T., Lupu, M.G., Simon, S., Sandu, S.G., Mierla, M., Rusu, M.V.: 2010, Study of coronal jets during solar minimum based on STEREO/SECCHI observations. *Solar Phys.* **264**, 365. DOI. ADS.
Roberts, B., Edwin, P.M., Benz, A.O.: 1984, On coronal oscillations. *Astrophys. J.* **279**, 857. DOI. ADS.
Robertson, D., Ruderman, M.S.: 2011, Resonantly damped oscillations of two coronal loops. *Astron. Astrophys.* **525**, A4. DOI. ADS.
Rosenberg, H.: 1970, Evidence for MHD pulsations in the solar corona. *Astron. Astrophys.* **9**, 159. ADS.
Ruderman, M.S., Erdélyi, R.: 2009, Transverse oscillations of coronal loops. *Space Sci. Rev.* **149**, 199. DOI. ADS.
Ruderman, M.S., Roberts, B.: 2002, The damping of coronal loop oscillations. *Astrophys. J.* **577**, 475. DOI. ADS.
Savcheva, A., Cirtain, J., Deluca, E.E., Lundquist, L.L., Golub, L., Weber, M., Shimojo, M., Shibasaki, K., Sakao, T., Narukage, N., Tsuneta, S., Kano, R.: 2007, A study of polar jet parameters based on hinode XRT observations. *Publ. Astron. Soc. Japan* **59**, S771. DOI. ADS.
Schrijver, C.J., Aschwanden, M.J., Title, A.M.: 2002, Transverse oscillations in coronal loops observed with TRACE I. An overview of events, movies, and a discussion of common properties and required conditions. *Solar Phys.* **206**, 69. DOI. ADS.
Schrijver, C.J., Title, A.M., Berger, T.E., Fletcher, L., Hurlburt, N.E., Nightingale, R.W., Shine, R.A., Tarbell, T.D., Wolfson, J., Golub, L., Bookbinder, J.A., Deluca, E.E., McMullen, R.A., Warren, H.P., Kankelborg, C.C., Handy, B.N., de Pontieu, B.: 1999, A new view of the solar outer atmosphere by the transition region and coronal explorer. *Solar Phys.* **187**, 261. DOI. ADS.
Shibata, K., Masuda, S., Shimojo, M., Hara, H., Yokoyama, T., Tsuneta, S., Kosugi, T., Ogawara, Y.: 1995, Hot-plasma ejections associated with compact-loop solar flares. *Astrophys. J. Lett.* **451**, L83. DOI. ADS.
Shimojo, M., Shibata, K.: 2000, Physical parameters of solar X-ray jets. *Astrophys. J.* **542**, 1100. DOI. ADS.
Srivastava, A.K., Dwivedi, B.N.: 2010, Signature of slow acoustic oscillations in a non-flaring loop observed by EIS/Hinode. *New Astron.* **15**, 8. DOI. ADS.

Terradas, J., Arregui, I., Oliver, R., Ballester, J.L., Andries, J., Goossens, M.: 2008, Resonant absorption in complicated plasma configurations: Applications to multistranded coronal loop oscillations. *Astrophys. J.* **679**, 1611. DOI. ADS.

Uchida, Y.: 1970, Diagnosis of coronal magnetic structure by flare-associated hydromagnetic disturbances. *Publ. Astron. Soc. Japan* **22**, 341. ADS.

Van Doorsselaere, T., Ruderman, M.S., Robertson, D.: 2008, Transverse oscillations of two parallel coronal loops. *Astron. Astrophys.* **485**, 849. DOI. ADS.

Verwichte, E., Foullon, C., Van Doorsselaere, T.: 2010, Spatial seismology of a large coronal loop arcade from TRACE and EIT observations of its transverse oscillations. *Astrophys. J.* **717**, 458. DOI. ADS.

Verwichte, E., Aschwanden, M.J., Van Doorsselaere, T., Foullon, C., Nakariakov, V.M.: 2009, Seismology of a large solar coronal loop from EUVI/STEREO observations of its transverse oscillation. *Astrophys. J.* **698**, 397. DOI. ADS.

Wang, T., Ofman, L., Davila, J.M., Su, Y.: 2012, Growing transverse oscillations of a multistranded loop observed by SDO/AIA. *Astrophys. J. Lett.* **751**, L27. DOI. ADS.

White, R.S., Verwichte, E.: 2012, Transverse coronal loop oscillations seen in unprecedented detail by AIA/SDO. *Astron. Astrophys.* **537**, A49. DOI. ADS.

Zimovets, I.V., Nakariakov, V.M.: 2015, Excitation of kink oscillations of coronal loops: Statistical study. *Astron. Astrophys.* **577**, A4. DOI. ADS.